ISSN 2042-8901 | Volume 15 | Issue 2

360 YEARS OF SCIENTIFIC PUBLISHING

INTERFACE FOCUS

Capillarity and Elastocapillarity in Biology

Theme issue 'Capillarity and Elastocapillarity in Biology' organized by David L. Hu, Ho-Young Kim and Dominic Vella.

THE ROYAL SOCIETY PUBLISHING

INTERFACE FOCUS

royalsocietypublishing.org/journal/rsfs

Research

Cite this article: Kim S, Tuazon H, Ha N, Tiwari I, Bhamla S, Hu DL. 2025 Flotation of aquatic worms and other hyponeuston. *Interface Focus* **15**: 20240057.
https://doi.org/10.1098/rsfs.2024.0057

Received: 15 December 2024
Accepted: 4 April 2025

One contribution of 8 to a theme issue 'Capillarity and Elastocapillarity in Biology'.

Subject Areas:
biomechanics

Keywords:
flotation, aquatic worm, meniscus, surface tension, regime diagram

Authors for correspondence:
Saad Bhamla
e-mail: saadb@chbe.gatech.edu
David L. Hu
e-mail: hu@me.gatech.edu

†These authors contributed equally to the study.

THE ROYAL SOCIETY PUBLISHING

Flotation of aquatic worms and other hyponeuston

Soohwan Kim[1,†], Harry Tuazon[2,†], Nami Ha[2], Ishant Tiwari[2], Saad Bhamla[2] and David L. Hu[1,3]

[1]George W. Woodruff School of Mechanical Engineering, [2]Chemical and Biomolecular Engineering, and [3]School of Biological Sciences, Georgia Institute of Technology, Atlanta, GA, USA

SB, 0000-0002-9788-9920; DLH, 0000-0002-0017-7303

The California blackworm, *Lumbriculus variegatus*, lives underwater and latches its tail to the water surface for respiration and stability. Little is known about the upward force generated by this posture. In this combined experimental and theoretical study, we visualize the menisci shape for blackworms and blackworm mimics, composed of smooth and corrugated epoxy rods. We apply previous theoretical models for floating cylinders to predict the upward force and safety factor of blackworms as well as other organisms such as mosquito larvae, leeches and aquatic snails. Understanding the upward forces of organisms that latch onto the water surface may help to understand the evolution of interfacial attachment and inspire biomimetic robots.

1. Introduction

While freshwater lakes and rivers cover only 2.5% of the earth's surface, many smaller bodies of water like ponds and creeks can support an astonishing diversity of life at the water surface. Organisms that spend their entire life cycle within a few centimetres *below* the air–water surface are called hyponeuston [1], while those that navigate *above* the water surface are known as epineuston [2,3]. Some organisms, like whirligig beetles, blur the line between hyponeuston and epineuston by swimming half-submerged [4]. The region inhabited by hyponeuston is a 'critical biotope' because it is home to many larval and juvenile species. Hyponeuston are subject to environmental natural challenges such as heavy rain, sunlight and evaporation. Increasingly, they also face pollution such as oil spills or heavy metal runoff. Since many species depend on hyponeuston for survival, understanding the physical adaptations of hyponeuston can play a critical role in conservation. Epineuston like the water strider [5] and hyponeuston like the water boatmen [6,7] have inspired biomimetic robots which are envisioned to play a role in aquaculture and environmental monitoring [8]. The goal of this article is to apply theoretical models of floating cylinders to predict flotation of elongate biological organisms. Passive flotation helps keep these animals in place in their preferred habitat and reduces the energy required to actively swim to stay afloat.

In this study, we focus on elongate animals with at least two of their characteristic dimensions being smaller than the capillary length, $l_c = \sqrt{\sigma/(\rho_f g)}$, typically 2.7 mm for water, where σ is the surface tension, ρ_f is the density of water and g is gravity. Bodies much larger than this size float via buoyancy. By Archimedes' principle, large buoyant objects have an effective density less than that of water. Boats and ducks reduce their effective density by having a waterproof exterior that traps air pockets. Bodies smaller or comparable to the capillary length may be denser than water and still float by exploiting surface tension. In fact, by the deployment of hydrophilic and hydrophobic body parts, both hyponeuston and epineuston have evolved diverse ways to float and propel themselves at the water surface. For example, the Australian water scavenger beetle (Hydrophilidae) [9], backswimmer [10] and the water snail [11] all

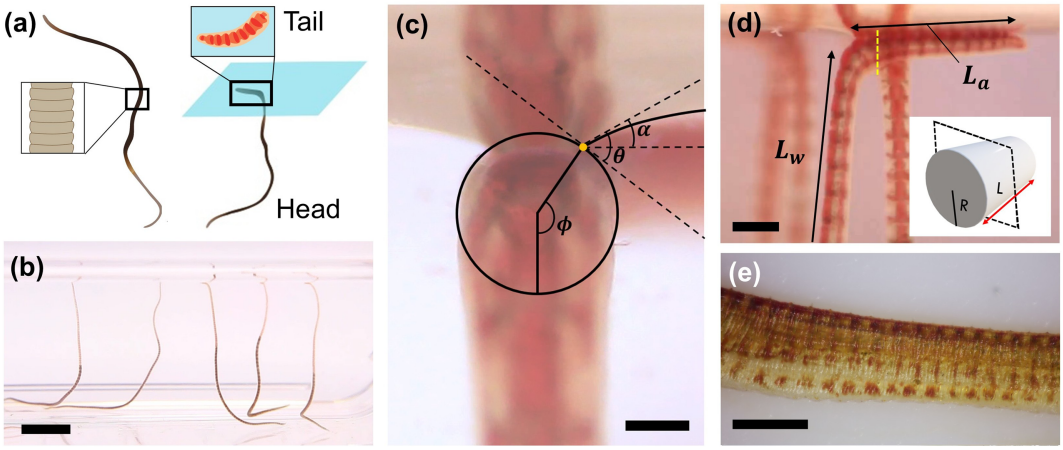

Figure 1. (a) Drawings of California blackworms highlighting body corrugations and their tails used as a latch at the water surface. (b) Blackworms voluntarily latching themselves to the water surface in order to respire in the lab. Scale bar 10 mm. (c) Cross-section of blackworm tail at the water surface. The three angles depicted are: θ (contact angle), ϕ (wetting angle) and α (meniscus angle). The triple point is marked with a yellow dot. Scale bar 200 µm. (d) An L-shaped aquatic worm floating at the air–water interface. The yellow dashed line represents the cross-section in (c). Scale bar 500 µm. (e) Microscopic view of the worm's ridges, captured while the worm was outside the water tank. Scale bar 400 µm.

propel themselves inverted beneath the interface. Mosquito eggs and larvae are hyponeuston that cling to the interface during their development [12,13]. Midge larvae use adhesive discs to both adhere to the underside of the water surface and act as a rudder [14].

Comparatively less is understood of the mechanics of elongate hyponeuston that may adjust their length of contact with the water surface. We begin our study with the California blackworm, *Lumbriculus variegatus*, shown in figure 1, which exhibits oxygen-gathering behaviours distinct from its typical submerged foraging activity [15]. Hyponeuston often possess a specialized posterior organ called a siphon, which functions as a respiratory appendage. In some species, the siphon is relatively short, for example, about half the body length in mosquito larvae [12], while in others, such as the rat-tailed maggot (larvae of *Eristalis*), it is long and flexible, extending up to twice the body length [16]. While blackworms do not possess a siphon and primarily respire by absorbing dissolved oxygen from the water column, they can supplement oxygen intake through their skin by positioning their tails at the air–water interface [17–19]. This behaviour involves extending their tails to the interface while remaining suspended off the floor, then flexing the posterior segments to form a 90-degree 'latch.' This latch hangs on the water surface, exposing a segment of the worm to the air, enabling direct oxygen uptake. Since only a small fraction of their body is attached, blackworms can quickly detach from the interface to escape potential threats (figure 1a,b) [15,20–22].

The dynamics and statics of cylinders at the water surface have long been of interest to predict water entry, sinking, and jumping from the water surface [23,24]. We were particularly inspired by the theoretical predictions of Vella *et al*. [25] for the depth of cylindrical floating objects, which we believe could be applied to understanding flotation of California blackworms.

The goal of this work is to understand the flotation of blackworms and other aquatic hyponeuston, which have received less attention than epineuston. The surface of California blackworms consists of ridges, shown in Figure 1d,e, whose function motivated us to consider the hydrodynamics of flotation. We apply the model by Vella *et al.* to create a quantitative framework for flotation at the water surface. Our study was guided by a hypothesis that the ridges of blackworms enhance flotation by increasing the wetted perimeter and generating additional vertical surface tension forces. Our findings lead us to reject this hypothesis, as further elaborated in the discussion section.

We begin with the experimental and mathematical methods for studying flotation of elongate objects. Then we present observations of the geometry of blackworms and describe their floating position below the water surface. Using Vella *et al.*'s model, we determine the regime of flotation, calculate how much capillary or buoyancy forces are used by blackworms, and their safety factor for flotation. We then present experiments with smooth and corrugated cylinders, which we use as physical mimics of the blackworm. Lastly, we apply our theoretical framework to consider the safety factor of other small floating organisms and address the utility of the corrugations on the blackworm's skin.

2. Material and methods

2.1. Construction of worm mimics

We construct worm mimics, composed of cylinders of varying density ρ_s to explore the various regimes of flotation. We fabricated two kinds of cylinders, one of poly-epoxy and other with a polycarbonate shell and poly-epoxy filler. The differing shells of the cylinders allow us to explore the use of different contact angles for flotation. The diameter of the samples was 5 mm, approximately 10 times larger than that of blackworms. Since the theoretical model is for a two-dimensional cylinder, we made the cylinder sufficiently long (length $L = 20D$) to minimize end effects.

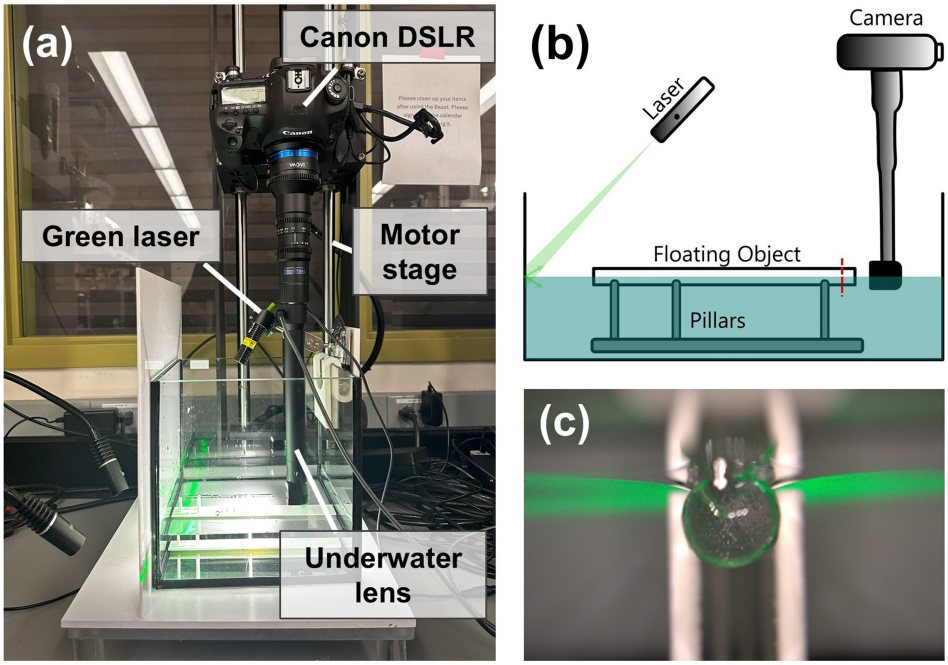

Figure 2. (a) Experimental setup for filming worm mimics. (b) Schematic of the setup highlighting the camera, laser, and floating cylinder. The red dashed line represents the cross-section in (c). (c) Cross-sectional view showing the meniscus, where the green laser light reflects off the back wall and illuminates the meniscus.

For the epoxy cylinders, disposable plastic straws (Zmaxqii, China, black), of both smooth and corrugated shapes, were used as moulds. For the polycarbonate cylinders, polycarbonate pipes (Meccsnixity Co., ID 5 mm and OD 245 mm) were cut into 10 cm segments using a plastic pipe cutter (Libration Co.). The pipes were filled with the epoxy-steel string mixture following the same procedure as the epoxy samples.

Epoxy resin and hardener were combined in a 1:1 volume ratio and mixed for 5 min to ensure even distribution. After mixing, the epoxy was left undisturbed for 10 min to reduce bubble formation. The mixture was then drawn into a syringe with a 16-gauge, 1.5-inch needle and carefully injected into 10 cm-long plastic straws with either smooth or corrugated surfaces. During curing, piano steel strings, of diameter ranging from 0.2 to 1 mm, were gently placed into the epoxy to create samples with the desired density.

The corrugated plastic straws were often found to be deformed after hardening. We thus 3D-printed a shelf system to keep a set of three straws straight during hardening. To facilitate the removal of the straw samples, adhesive tape was applied to the inner surface of the 3D-printed shelf. Curing took place in two stages. After 7 h, the initially moulded epoxy was topped up to the edge of the cylinders to create flat end caps. After a total curing period of 48 h, the samples with tapes were removed from the shelf system, then the straws and tapes were removed from the epoxy cylinder using a cutter.

Even with our best efforts, the epoxy did not fully fill the moulds. Thus, to make a more accurate estimate of the density of the cylinders, we used water volume displacement in 5 ml (OD 8 mm) and 10 ml (OD 9.5 mm) serological tubes (Fisher brand), with one end of each tube sealed using thermoplastic adhesive.

2.2. Imaging

Our experiments involved placing cylinders, worms and other organisms on the water surface, and photographing the ensuing meniscus shape. Cylinders were immersed in DI water while organisms were immersed in the water they were reared in.

To assess the surface wettability of the epoxy and polycarbonate cylinders, we used several methods. We first used a contact angle goniometer (Ramé-hart 210) to measure the contact angle θ on a flat sample of polycarbonate and a flat mould of epoxy. Possibly due to contact angle hysteresis, we found that this contact angle was not an accurate measure of the contact angle of the cylinders. Thus, in our modelling, we used image analysis to measure the contact angle θ.

To visualize the meniscus shape, we used the underwater camera setup shown in figure 2. A DSLR camera (Canon EOS 5DS R) was mounted on a motorized stage to control its vertical position. The camera was equipped with an underwater lens (Laowa FF 24 mm Macro PeriProbe) with built-in LED lighting. The camera setup was calibrated to maintain consistent alignment, with the centre of the underwater lens positioned 1 mm below water level. We incorporated a green sheet laser directed at the background to enhance the visibility of the meniscus. We 3D-printed platforms with five surrounding pillars to stabilize the cylinders during filming. The water level was adjusted so that the pillars prevented the cylinders from drifting due to air currents. After the platforms were submerged, the meniscus profiles remained undisturbed provided there was a separation between the platform and pillars. We photographed both ends of the cylindrical samples, rotating them 180 degrees between each photo. The wetting angles ϕ were measured from photographs using Image J by fitting the cylinder with a circle and drawing a line towards the triple point.

We captured footage of aquatic animals, using a combination of two lenses (Canon RF24-70mm F2.8 L IS USM lens and Mitutoyo M Plan Apo 10× microscopic lens) for top-view and side-view.

2.3. Animal preparation

We procured California blackworms (*L. variegatus*) from Ward's Science (Rochester, NY). The blackworms came with freshwater leeches (*Helobdella sp.*). Rearing conditions for worms and leeches are the same as described in our earlier publications [18,19]. We also procured black planarians (*Phagocata gracilis*) from Ward's Science, which were reared in a separate container with similar conditions to the worms. Planarians were fed with blackworms once a week. Freshwater snails were incidentally obtained when we purchased duckweed (*Lemna spp.*) from Ward's Science (Rochester, NY, USA). The snails were identified visually and used opportunistically in the experiments. Also, we used 1-week-old larvae of yellow fever mosquitos (*Aedes aegypti*) hatched from dry-state lab-grown eggs obtained from the Malaria Research Center from the Center of Disease Control. The larvae were raised in water and fed commercial fish food.

The density of various animals was measured using volume displacement in a 1 ml flask (Pyrex® volumetric micro flask). To establish a calibration curve, we first recorded the water level in the flask at several known volumes of de-inoized (DI) water. For volume measurements, a group of animals was introduced into the flask, and the change in water level was measured after their removal. The weight of the group of animals was measured using an electronic balance. To account for the film of water on the surface of the animals, their surface was wiped, and their dry weight was subsequently recorded to calculate the density. Throughout the procedure, soft-grip-compliant tweezers were used to handle the animals.

3. Mathematical model

We reprint here the model derived by Vella *et al.* [25] for the net force of a floating cylinder.

3.1. Force balance

Consider a cylinder of radius R and length L sitting statically on the air–water interface as shown in figure 1c. The cylinder deforms the water surface and its weight F_g is supported by some combination of capillary force F_c and buoyancy F_b [23,25–27]. Keller's extended Archimedes principle states that the sum of the buoyancy and capillary forces for a floating body is equal to the weight of the fluid displaced within and outside of the contact line, respectively [28]. Vella *et al.* [25] write the weight, capillary force, and buoyancy force as:

$$F_g = (\text{volume of cylinder}) \cdot \rho_s g = \pi R^2 L \rho_s g, \tag{3.1}$$

$$F_c = (\text{contact perimeter}) \cdot \sigma \sin\alpha = 2L\sigma \sin\alpha, \tag{3.2}$$

$$\begin{aligned} F_b &= (\text{volume displaced by meniscus within contact lines}) \cdot \rho_f g \\ &= (2R \sin\phi z_c + \phi R^2 - \frac{1}{2} R^2 \sin(2\phi)) L \rho_f g, \end{aligned} \tag{3.3}$$

where ϕ is the wetting angle, which indicates how much of the cylinder is wetted. The wetting angle ϕ is measured from the bottom of the cylinder and thus $\phi = \pi$ corresponds to the cylinder completely submerged (we report angles in both radians and degrees, as specified, in this study). The contact angle of water on the cylinder θ is a material property but is likely to have a range of angles due to contact angle hysteresis, and we use the advancing contact angle θ_a from experiments. The meniscus angle α is the angle between the meniscus and the horizontal. The meniscus depth z_c is measured between the triple point and the original unperturbed water surface. The density of the solid cylinder is ρ_s. Figure 1c illustrates the side view of the floating cylinder. Geometric compatibility gives the constraint

$$\phi = \alpha + \pi - \theta, \tag{3.4}$$

which implies that for a given material and thus a constant contact angle, the wetting angle ϕ is dependent on the meniscus angle α. Thus, for a given cylinder material, we can list ϕ as the single variable that dictates the cylinder's position underwater. The net vertical force $F_{net} = F_c + F_b - F_g$ will be zero at equilibrium. We proceed by normalizing the net vertical force by σL to write the dimensionless net vertical force, $\bar{F}_{\text{net}}$,

$$\bar{F}_{\text{net}} = 2\sin\alpha + \frac{\rho_f g R^2}{\sigma} \left(2\sin\phi \frac{z_c}{R} + \phi - \frac{1}{2}\sin(2\phi) - \frac{\rho_s}{\rho_f}\pi \right) = 0, \tag{3.5}$$

where under equilibrium, $\bar{F}_{net} = 0$. The above equation contains two dimensionless numbers, Bo and SG:

$$\text{Bo} = \frac{\rho_f g R^2}{\sigma} = \frac{\text{buoyancy}}{\text{surface tension}} \qquad \text{SG} = \frac{\rho_s}{\rho_f} = \frac{\text{solid density}}{\text{water density}}. \tag{3.6}$$

The Bond number, Bo, is the ratio of the buoyancy force to the surface tension force. It is also equivalent to the squared ratio of cylinder radius and capillary length l_c. The specific gravity, SG, is the ratio of the solid density to the water density.

3.2. Meniscus profile

The shape of the meniscus is given by the Young-Laplace equation, a vertical force balance at every point, where hydrostatic pressure equals curvature pressure: $\rho g z = -\sigma \nabla \cdot \mathbf{n}$ where $\mathbf{n}$ is the outward normal to the water surface [27,29]. Non-dimensionalizing

this equation by the capillary length and solving for the curvature $\nabla \cdot \mathbf{n}$ yields the differential equation for the two-dimensional meniscus profile $z(x)$

$$\frac{z_{xx}}{(1+z_x^2)^{3/2}} = z, \tag{3.7}$$

which may be integrated using boundary conditions at the triple point and the infinite free surface to write the depth of the cylinder z_c [27]:

$$\frac{z_c}{R} = \sqrt{\frac{2(1-\cos\alpha)}{Bo}}. \tag{3.8}$$

3.3. Perimeter of corrugated cylinder

In this section, we aim to quantify the impact of surface corrugation on the wetted perimeter of a floating cylinder, as the magnitude of surface tension is proportional to the perimeter in general. We calculate the intersection perimeter between a corrugated cylinder and a plane at a given height.

Consider a corrugated cylinder with an average radius R and a sinusoidal corrugation of amplitude A along the z-axis. Assuming corrugation amplitude is smaller than cylinder radius ($A < R$), the equation is:

$$x^2 + y^2 = (R + A\sin(2\pi z/\lambda))^2, \tag{3.9}$$

where λ is the wavelength of the sinusoidal pattern. Then we consider the perimeter of the intersection of this corrugated cylinder with a plane $y = y_0$.

$$x = \pm\sqrt{(R + A\sin(kz))^2 - y_0^2}, \tag{3.10}$$

where $2\pi/\lambda$ is substituted by the wave number k. This defines the x-coordinate of the curve of intersection for each value of z. For equation (3.10) to be physically meaningful, the expression inside the square root must be non-negative, imposing the condition,

$$R + A\sin(kz) \geq y_0. \tag{3.11}$$

This constraint ensures that the intersection exists for a given y_0. If y_0 exceeds the local radius at any point, the intersection vanishes, leading to the formation of separate wetted islands. The critical height at which this separation occurs is $y_0 = R - A$.

To find the perimeter of the intersection, we compute the arc length of the curve described by parametric equations $x(z)$ and $y(z)$ over an interval $z_1 \leq z \leq z_2$ which is given by:

$$L = \int_{z_1}^{z_2} \sqrt{\left(\frac{dx}{dz}\right)^2 + \left(\frac{dy}{dz}\right)^2 + 1}\, dz. \tag{3.12}$$

Since $y = y_0$ is constant, $\frac{dy}{dz} = 0$. Differentiating x with respect to z, we apply the chain rule:

$$\frac{dx}{dz} = \frac{(R + A\sin(kz)) \cdot Ak\cos(kz)}{\sqrt{(R + A\sin(kz))^2 - y_0^2}}. \tag{3.13}$$

Equations (3.12) and (3.13) are only applicable for a single continuous perimeter. In case of multiple islands, the limits of integration need to be adjusted so that the function integrates only if the integrand is not imaginary. From equation (3.11),

$$z = \frac{1}{k}\sin^{-1}\left(\frac{y_0 - R}{A}\right). \tag{3.14}$$

We obtain two solutions, z_1' and z_2'. Therefore, the total perimeter of multiple islands is:

$$L = n\int_{z_1'}^{z_2'} \sqrt{\left(\frac{dx}{dz}\right)^2 + \left(\frac{dy}{dz}\right)^2 + 1}\, dz, \tag{3.15}$$

where n is number of islands, which can be approximated by $(z_2 - z_1)/\lambda$.

4. Results

4.1. Safety factors of hyponeuston

A typical resting posture for California blackworms in captivity is the inverted L-shaped posture shown in figure 1d, where the worm latches a tail segment of length $L_a = 1.52 \pm 0.65$ mm to the water surface and suspends the remainder of its body, of length L_w vertically below. Since the worm's total length $L_{total} = L_a + L_w$ is 30.2 ± 7.4 mm, the latched section is only 1/20th the length of its whole body, giving it an ability to quickly detach from the water surface and dive if it is in danger. The inset in the figure shows a

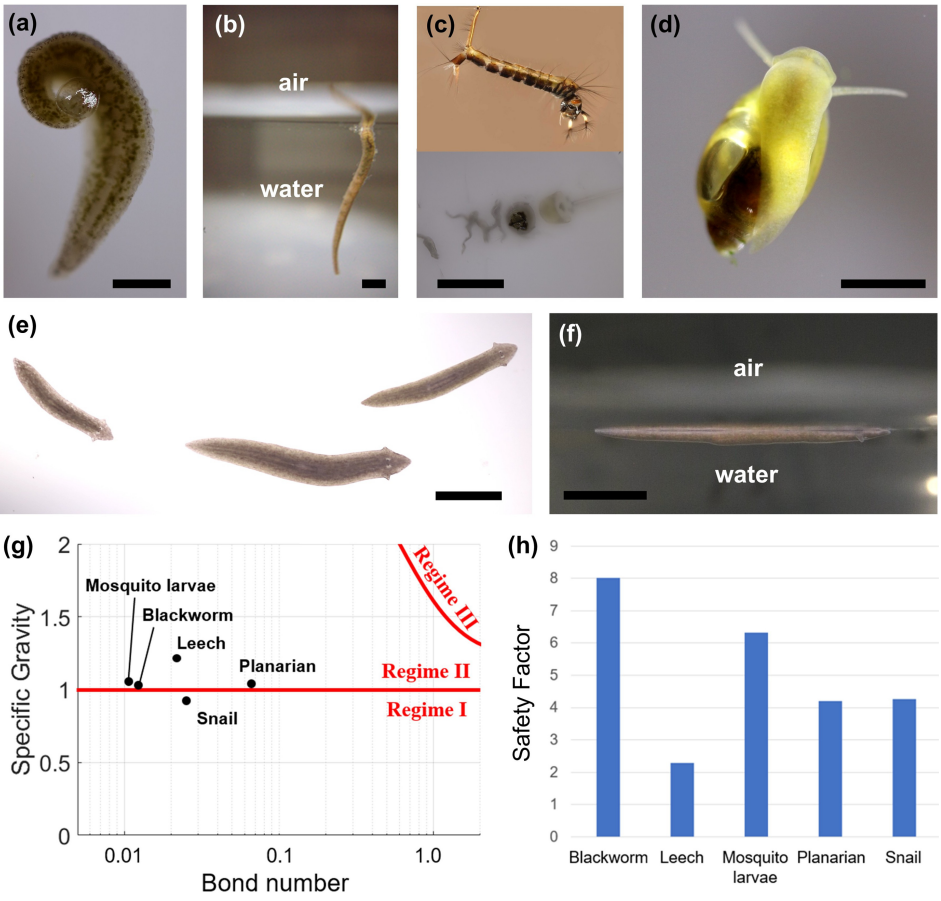

Figure 3. Top and side view images of various hyponeuston at the air–water interface. (a, b) Leech (*Helobdella sp.*). Scale bar 1 mm. (c) Mosquito larvae. Top, *Culex erraticus*. Image courtesy of Nathan Burkett-Cadena, UF/IFAS. Bottom, *Aedes agypti*. Scale bar 1 mm. (d) Snail inverted at the water surface. Scale bar 1 mm. (e, f) Planarian. Scale bar 3 mm. (g) The regime diagram of flotation with corresponding points with different aquatic animals. (h) Comparison of safety factors across animals.

cross-section of the tapered latch, with diameter $D = 0.6 \pm 0.1$ mm at its widest section. The diameter is comparable to the capillary length, indicating the dominance of surface tension forces in weight support. Before we precisely calculate the flotation force, we can estimate the force using scaling arguments.

We measured the density ρ and apparent perimeter P associated with five species of hyponeuston, including blackworms, leeches, planaria, mosquito larvae and snails (figure 3a-f). By apparent perimeter, we mean the perimeter that we can measure without a microscope because the actual perimeter may be greater due to microscopic features. The surface tension force scales as σP, and assuming Archimedes law of a fully submerged object, the buoyancy force may be written $\rho_f V g$ where V is the submerged volume of the body. These forces support the body weight, denoted by w. The ratio of the upward forces to the weight may be written as the safety factor SF [30]:

$$SF = \frac{\text{surface tension + buoyancy}}{\text{body weight}} = \frac{\sigma P + \rho_f V g}{w}. \tag{4.1}$$

A safety factor or $SF = 1$ indicates the combined surface tension and buoyancy balances the animal's weight. Any additions to its weight will cause it to sink. A safety factor greater than 1 indicates that the animal is safe from sinking. It may take on extra weight, or otherwise rise out of the water thereby reducing its perimeter P or submerged volume V. Equation (4.1) neglects the influence of contact angle and assumes that the object is superhydrophobic. It also neglects the vertical position of the object, which we consider carefully later.

In addition to safety factor, we can calculate a more common dimensionless group, the Bond number $Bo = \rho_f g R^2/\sigma$ which relates the radius R of the animal's cross-sectional area to the capillary length. The relationship between SG and Bond number is shown in figure 3g. Regime I indicates animals that float by buoyancy, and regime II indicates animals that float by surface tension. Only a single animal, the snail, uses buoyancy to float.

Using volume displacement and measurement of mass, we measure the density of the blackworm, which is slightly higher than that of water, at $\rho = 1.025 \pm 0.002$ g/cm^3. Based on the length of its latched tail, the bloodworm has a safety factor of 8.0. Thus the tail of the blackworm supports eight times its weight. Since the blackworm is just slightly denser than water: it only needs to latch a small portion of its tail for support.

A mosquito larva attaches to the surface with just its syphon, suspending its body vertically below, as shown in figure 3c. The larva has a density of 1.04 ± 0.015 g/cm^3, and a large safety factor of 6.3. Leeches (figure 3a,b) are denser ($\rho = 1.211 \pm 0.031$ g/cm^3) and when they attach to the water surface with their sucker, they have a low safety factor of 2.3. As shown in figure 3e,f, the planarian attaches its whole body to the water surface and has a thin body. It has a safety factor of 4.2.

Table 1. Measured physical and dimensionless properties of small aquatic organisms. Parameters include body radius, perimeter, mass, volume, specific gravity (SG), Bond number (Bo) and flotation safety factor.

species	R (cm)	P (cm)	mass (g)	volume (cm^3)	SG	Bo	safety factor
blackworm	0.030	0.670	0.007	0.007	1.025	0.012	8.01
leech	0.040	0.218	0.011	0.009	1.211	0.022	2.28
mosquito larvae	0.028	0.131	0.002	0.002	1.036	0.011	6.32
planarian	0.070	0.467	0.011	0.010	1.031	0.067	4.20
snail	0.043	0.403	0.009	0.010	0.922	0.025	4.25

While snails float upside down on the water surface (figure 3d), they don't need to keep their foot attached to the water surface because they are buoyant with a density of 0.922 ± 0.102 g/cm^3. However, we note that the snail's air pockets are in its shell, so without the surface tension forces acting on its foot, the snail's shell would flip and the snail would float shell-side-up. Moreover, the snail can regulate its density by letting water into its shell. Based on the amount of water the snail had at the time of density measurement, its safety factor is 4.3. Overall, the blackworm demonstrated the highest safety factor among the investigated animals, achieving this by utilizing only 5% of its body length. If the entire body length were used for support, the safety factor could increase dramatically to 141.6. The physical properties and dimensionless number of the organisms are listed in table 1.

The above arguments are only a rough estimate of the anchoring force on hyponeuston. They do not take into account the vertical position of the organism under the water surface. They also neglect microscopic roughness, such as the ridges on the worm, which increase the perimeter and potentially the safety factor. To test our hypothesis about corrugations increasing weight support, we conduct experiments with blackworms and cylindrical mimics of the blackworms.

4.2. Flotation of blackworm mimics

We proceed with a more accurate two-dimensional model that incorporates the worm's corrugations, contact angle, and vertical position below the water surface. First, we justify our two-dimensional model. Figure 1c shows the tail as a cone of diameter D that tapers to a point across the latch length L_a. The angle of tapering may be written $\beta = \tan^{-1}\frac{D}{2L_a} = 11°$, which is small. When the worm is latched, the tapering causes the centre line of the worm to be inclined by angle β to the horizontal. Our model and experiments neglect both the tapering and the incline: instead, we model the worm as if it were a horizontal cylinder of width equal to the latch's largest width, marked by the dashed yellow line in figure 1d. Since we analyse the wider and more submerged section of the tilted cylinder, our calculations below will overestimate the supporting force.

Using an underwater camera oriented along the worm's centre line and facing the widest part of the worm's latch, we can accurately measure the worm's widest cross-section, as shown in figure 1c. The triple point, where the worm, water and air meet, is marked by a yellow dot, from which emerge three angles: the contact angle $\theta = 61 \pm 6.6°$ ($n = 4$), wetting angle $\phi = 138.9 \pm 6.5°$ ($n = 33$) and meniscus angle $\alpha = 19.9 \pm 9.27°$ [17]. The wetting angle ϕ indicates how deeply underwater the worm is submerged; the contact angle is a material property; and the meniscus angle relates the angle of the meniscus to the horizontal at the contact point.

Figure 1e shows the worm's tail corrugation when exposed to air, as photographed with a microscope. The sinusoidal corrugations have amplitude $A = 7.4 \pm 3.9$ µm and wavelength $\lambda = 113.7 \pm 11.7$ µm, respectively. Given the exposed length L_a, the number of exposed body segments $N = L_a/\lambda = 13$. Normalizing these values by the worm diameter D, we obtain a dimensionless amplitude of $A/D = 0.016 \pm 0.008$ and a dimensionless wavelength $\lambda/D = 0.252 \pm 0.016$. We will consider these values in the discussion.

To investigate the effects of the corrugations on the flotation of the worm, we fabricate mimics of the worm at tenfold scale using cylinders of both smooth and corrugated texture. Equation (3.5) states the maximum net vertical force F_{net} on the cylinder for a given combination of Bond number and SG. This equation may be solved using the additional facts given in (3.4) and (3.8). Assuming the maximum possible capillary force, associated with $\theta = 90°$ and $\phi = 180°$, we can depict the space of possible solutions in the three-dimensional plot in figure 4a where the colours indicate the magnitude of the vertical force. A two-dimensional version of the same plot is given in figure 4b, where we separate the vertical forces into three regimes. Cylinders in Regime I float by virtue of buoyancy since the object is lighter than water. Cylinders in regime II float by a combination of buoyancy and surface tension. Cylinders in regime III sink. As we saw in figure 3g, there were no hyponeuston in regime III.

We construct 9 cylinders of polycarbonate and 14 cylinders of epoxy, with half of smooth and half of them corrugated surfaces and different weights. We placed the cylinders in water and measured their depth of submergence, which we report by the wetting angle ϕ. We expect heavier cylinders to sink deeper. This can be seen in figure 5c, which provides the corresponding experimental views at different SG values. Figure 5d depicts the schematics of the cylinder position and angles. As SG increases, so does α and ϕ, until the cylinder is completely submerged.

Figure 5a shows the wetting angle ϕ for smooth polycarbonate (PC) samples, with squares indicating experiments and the solid line indicating theory. The experiments are 4.8% higher than the theory but overall show good agreement. For theoretical calculations of ϕ, we used the cylinder's advancing contact angle ($\theta_{a,epoxy} = 79.4 \pm 8.2°$, $\theta_{a,PC} = 81.1 \pm 6.6°$) and the uncertainty in grey lines comes from the standard deviation of contact angle measurement. We had initially measured the static contact angles on flat surfaces of epoxy ($64.7 \pm 3.8°$) and PC ($82.7 \pm 4.2°$). However, these values were found not to match the experimental values

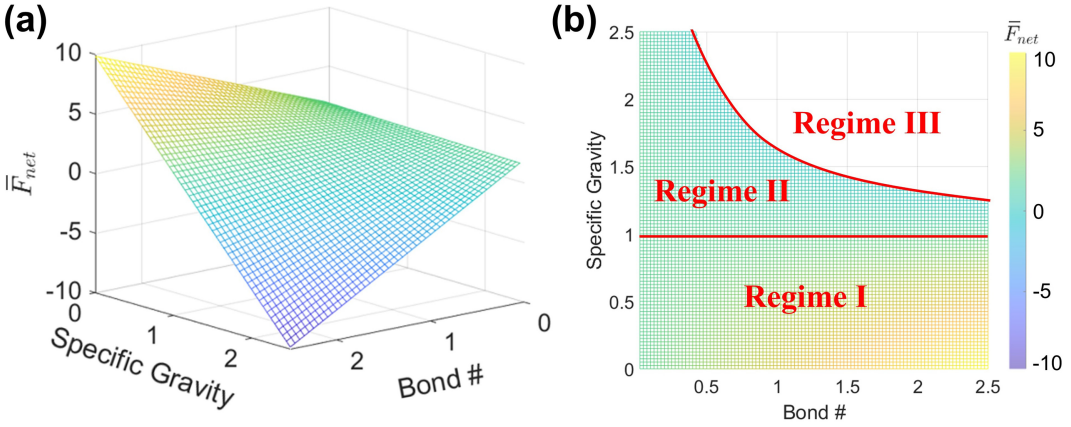

Figure 4. (a) A three-dimensional plot of the maximum net vertical force as a function of Bond number and specific gravity SG (assumes $\phi = 180°$, $\alpha = 90°$). (b) A two-dimensional plot of positive net vertical force regions (regions I and II) in which objects can float, and region III, where objects sink (assumed $\phi = 180°$, $\alpha = 90°$). The colourbar in (b) applies to both (a,b) and represents the dimensionless vertical net force.

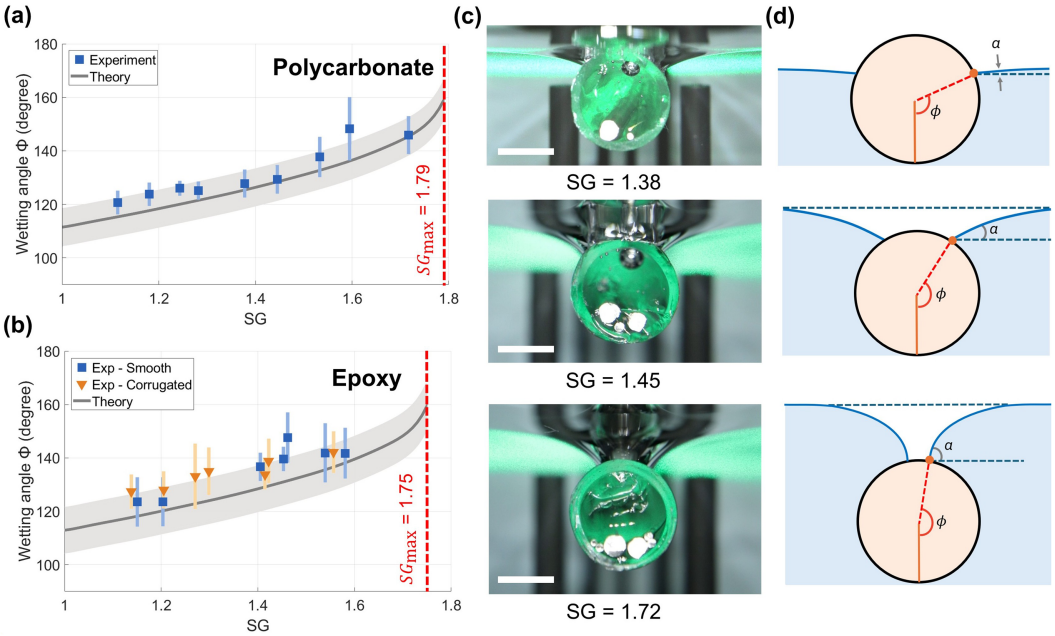

Figure 5. (a) The relationship between wetting angle ϕ and SG for smooth polycarbonate (PC) cylinders. (b) The relationship between wetting angle ϕ and SG for smooth and corrugated epoxy cylinders. (c) Experimental views of floating PC cylinders with SG values of 1.38, 1.45 and 1.72. Scale bars 3 mm. (d) Schematics illustrating the floating position of cylinders of increasing specific gravity.

observed on the cylinder. This makes sense because contact angle is also a function of surface roughness which depends on the manufacturing. The vertical dashed red line corresponds to the theoretical maximum SG for a cylinder of that size that can be supported on the water surface, as calculated by theory. Specifically, for polycarbonate and epoxy, the maximum SG = 1.79 and SG = 1.75, respectively.

Figure 5b presents the wetting angle for smooth (blue squares) and corrugated epoxy samples (orange triangles) along with the theory in grey. The average maximum diameter of corrugated samples was 5.65 mm, which is comparable to the diameter of the smooth samples (5.57 mm), ensuring they share the same theoretical predictions. The experiments again show slightly higher values than the theoretical predictions. Moreover, there was no significant difference in trend between corrugated and smooth cylinders, indicating that the corrugated cylinder does not support more weight than the smooth one.

4.3. Flotation of blackworm

Now that we have verified our model with floating cylinders, we apply it to our blackworm. The SG of the floating tail section is assumed to be the same as that of the blackworm, which is $SG = 1.025 \pm 0.002$. To consider the case of the worm holding only a partial length of its body on the water surface, we introduce the concept of modified SG. This assumes that the mass of the entire body is supported by the floating latch, leading to a modified $SG' = SG(L_w/L_a + 1) = 21.45$. Note that in figure 1b, the worm anterior is supported by the ground, which reduces the flotation force needed by the tail. However, the worms can easily float without touching the bottom when provided deeper water [17].

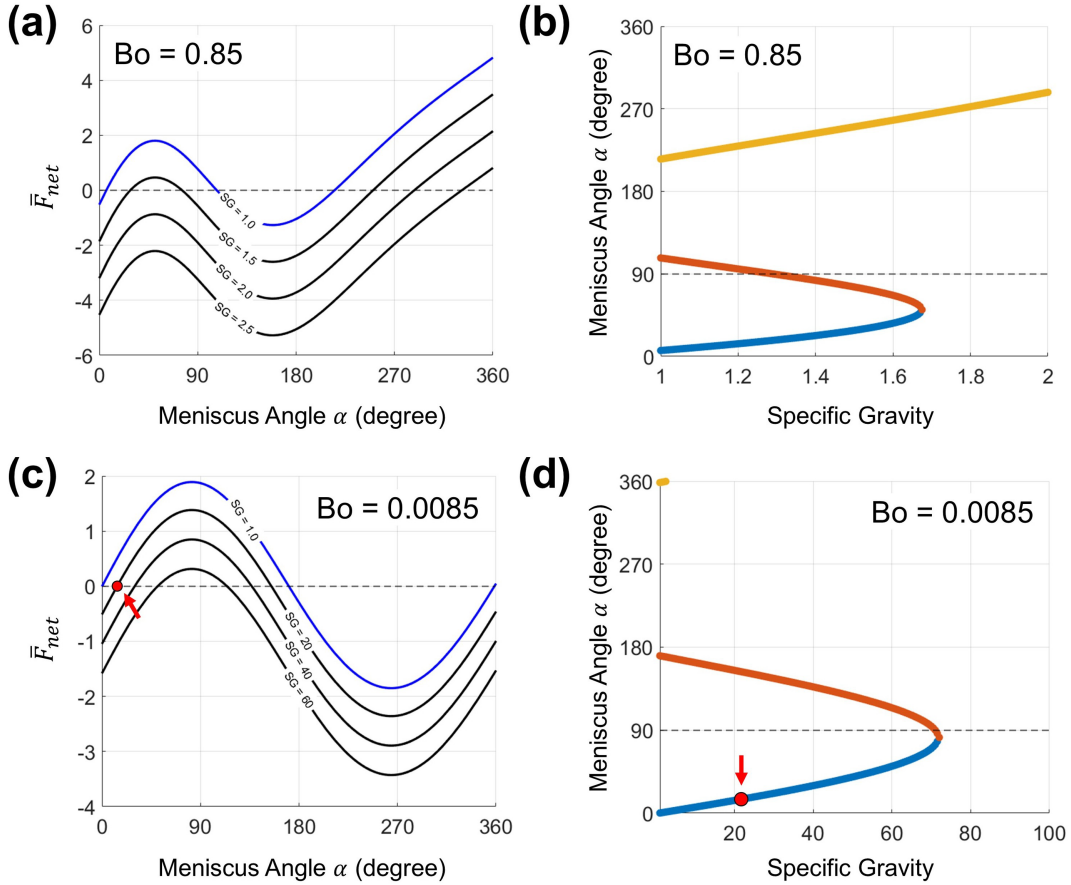

Figure 6. (a, c) Relationship between the dimensionless net force and meniscus angle α. The different curves denote specific gravity (SG) values . Bond number Bo is given in top of figure. For all, contact angle $\theta = 60°$. (b, d) The relationship between meniscus angle and specific gravity for zero net vertical force. The red dots indicate the equilibrium points corresponding to the blackworm (Bo = 0.0085, SG = 21.45). The solution exhibits a saddle-node bifurcation at the maximum specific gravity. The blue line represents the stable floating positions observed in experiments, while the red line corresponds to the unstable branch. The yellow line is a mathematical solution, where meniscus angles are not physically possible.

Now that we have measured $SG' \approx 20$ and Bo = 0.0085 we apply our theoretical framework to predict a meniscus angle for the worm. The worm's weight is supported by a combination of buoyancy and surface tension force. Equation (3.5) describes the relationship between the dimensionless vertical force $\bar{F}_{net}$ and the meniscus angle α for fixed values of SG and Bo. By iteratively solving for α using the condition $\bar{F}_{net} = 0$, we can predict the worm's floating position as a function of SG. Figure 6 illustrates the theoretical prediction on the dimensionless net force and meniscus angle for two different Bond numbers: part a-b corresponding to the worm mimic (Bo = 0.85) and part c-d corresponding to the blackworm (Bo = 0.0085). The number of solutions varies from one to three in the α range from 0 to 360°, depending on SG. As SG increases, the $\bar{F}_{\text{net}}$ curves shift downward, reducing the number of solutions, from three solutions to two to one. Note that it is not physical to have α= 360° so we consider an upper limit of 90°, for which the meniscus is vertical. In this range, the solution shows a bifurcation branching out from the maximum SG. As shown by the red data point corresponding to our worm observations, our theoretical prediction of 19.9 ± 9.3° does a good job of predicting the α for the worm, which from experiments is $\alpha = 15.1°$. Note the blue line corresponds to the observed floating position while the other lines (red and yellow) represent unobserved solutions. The blue line indicates the meniscus angle increases for denser objects.

Does the roughness of the worm increase its weight support? We saw from our earlier scaling arugment equation (4.1) that a corrugated cylinder will increase its perimeter relative to a smooth one, and potentially its weight support. Figure 7a shows the relationship between the contact perimeter and the height of the wetted perimeter from the cylinder centre. In this calculation, the corrugated cylinder has average radius R= 5 mm with corrugations of wavelength $\lambda = 2.5$ mm ($\lambda/R = 0.5$) and amplitude $A = 0.125$ mm ($A/R = 0.05$). As the smooth cylinder is submerged to greater depth, the wetted perimeter monotonically decreases, as expected. In contrast, as the corrugated cylinder is submerged, the perimeter increases due to the exposure of more peaks and valleys of the corrugations. The largest wetted perimeter occurs at a submergence depth of 0.238 cm, yielding a wetted perimeter of 7.18 mm. As the cylinder is submerged further, the island breaks up into multiple islands, each of which shrinks with increasing depth. The presence of multiple exposed islands was also observed when the worms floated at the interface (figure 7c, cover image for this issue). One might wonder if the observed islands were simply all underwater. However, we adjusted the lighting and observed that the white reflections are the islands where the worms are exposed to the air.

The increased perimeter with greater submersion depth, together with equation (4.1), suggests that the safety factor should increase. However, our experiments with corrugated mimics in figure 5 showed that this is not the case. We resolve this paradox by applying Keller's extended Archimedes theorem [28] to argue that a corrugated cylinder with radius R and corrugation amplitude

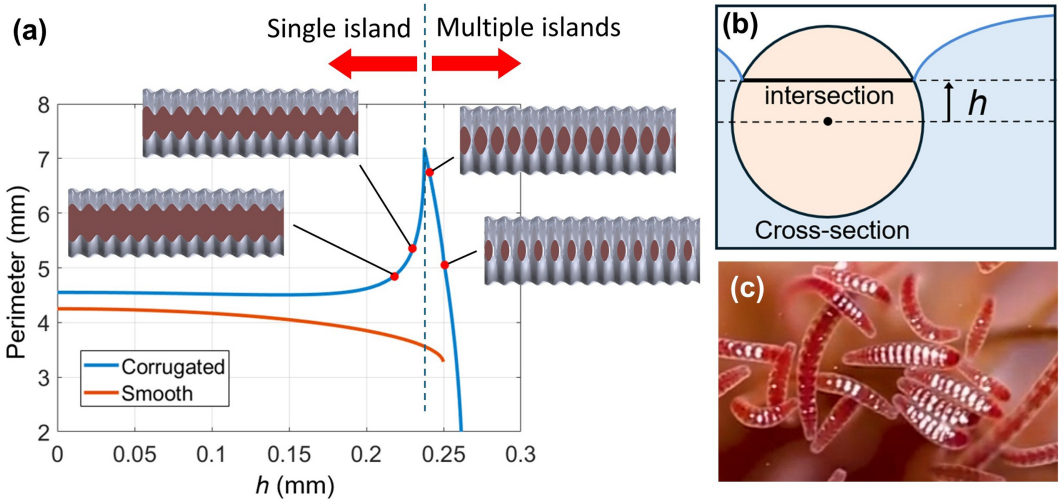

Figure 7. (a) The relationship between the theoretical contact perimeter and the depth of submersion, as measured between contact line and the cylinder centre. The insets are the cylinder's exposed area (in brown) to the air. (b) Schematic to define the submerged height *h*. (c) The observation of multiple islands during worm flotation.

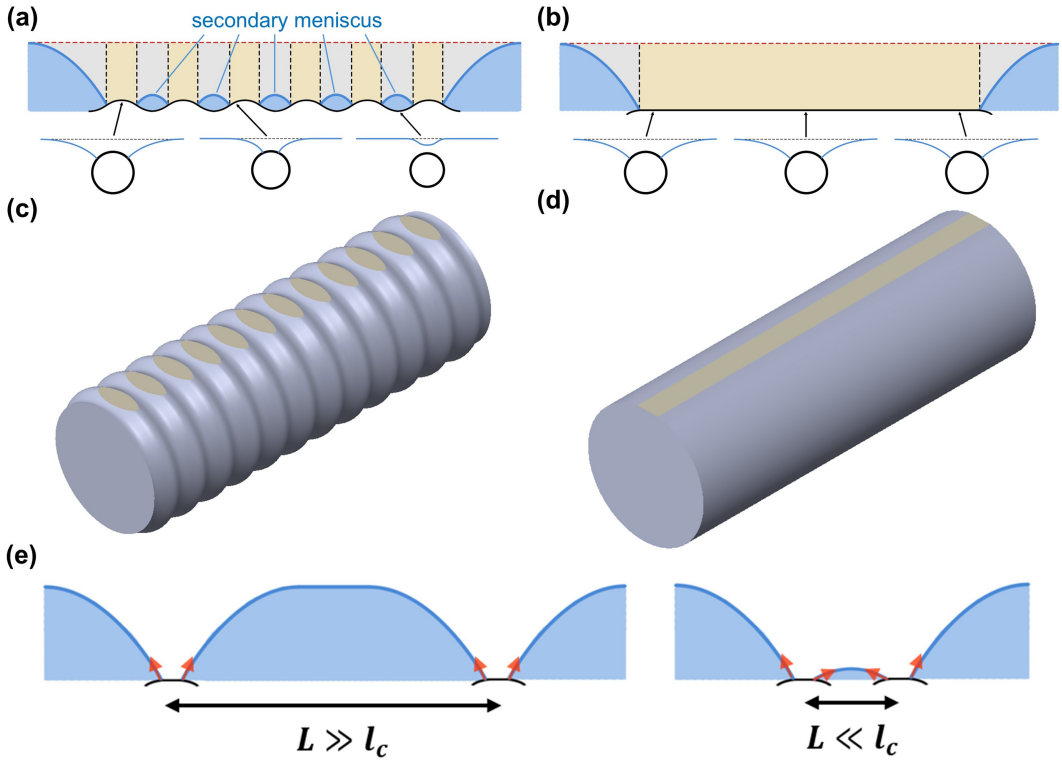

Figure 8. (a) Schematics of the side views of a floating corrugated cylinder, illustrating the formation of secondary menisci between the ridges. Insets show cross-sectional views. The grey and yellow areas indicate the contributions of surface tension and buoyancy to vertical support, respectively. (b) Schematics of the side views of a floating smooth cylinder, showing the absence of secondary menisci. (c,d) Three-dimensional view of corrugated cylinder (c) and smooth cylinder (d). The exposed area to the air is highlighted in yellow. (e) Behaviour of the secondary meniscus when two wetted islands are far apart (left) versus when they are close together (right). Here l_c is the capillary length.

A and wavenumber k will not have higher vertical force compared to a smooth cylinder of radius $R + A$. The key fact in resolving this paradox is that the corrugations are much smaller than the capillary length, as shown in figure 8e (right). If the corrugations were larger than the capillary length, then the cylinder is indeed increasing substantially in perimeter, and the menisci for each corrugation do not interact. In this case, shown in figure 8e (left), the weight support can increase.

The wavelength of the worm's corrugation is 0.125 mm, and the wavelength of the corrugated cylinder is 0.75 mm, both of which are significantly smaller than the capillary length of water, 2.7 mm. However, only well-spaced islands can generate higher support force. Figure 8 shows side views of the corrugated cylinder (part a) and smooth cylinder (part c). Grey regions indicate fluid volumes displaced outside the contact lines and yellow areas indicate fluid displaced above the exposed body. According to the Keller's theorem, the weight of the fluid in the grey region represents capillary force, and the weight of fluid in the yellow region is the buoyancy force. In the smooth cylinder, the meniscus has characteristic volume $L(R + A + l_c)l_c$ due to its characteristic depth l_c, length L of the cylinder, and width $R + A + l_c$. This volume represents the sum of the capillary and buoyancy force. In

the corrugated cylinder, the ridges create a greater proportion of weight support due to capillarity, but the total fluid displaced remains comparable between the two cases.

We thus disprove our hypothesis, finding that blackworm corrugations do not improve flotation. On the way, we demonstrate that one must be careful with scaling arguments for surface tension support of corrugated bodies. One must make certain that corrugations are separated by more than the capillary length if they are to increase weight support.

Although the ridges cannot help with weight support, they may help the worm to control its contact with the water surface. Each ridge represents a discrete contact with the water surface. The worm can adjust its flotation force by removing these contacts one-at-a-time, similar to filling a swim bladder in increments. In contrast, a worm without ridges would have continuous contact with the water surface, similar to the planaria. Adjusting such continuous contact may be more difficult to control. Finally, the ridges may have nothing to do with flotation and may simply be a matter of heredity. Members of the blackworm's family, Lumbriculidae, all have ridges to give their bodies the flexibility to burrow through sediment.

5. Discussion

Our main contribution in this work is determining the method of flotation for blackworms, which exhibit corrugations on their surface. We filmed the side view of floating cylinders to capture the depth of flotation of the worm and shape of meniscus, which are used to calculate the weight support. Few studies have filmed the static meniscus of floating objects. One study explored the dynamics of sinking glass cylinders, reporting the changing meniscus shape over time [23]. In previous work, the views of floating objects were mostly schematic diagrams. We encountered challenges in photographing due to the cylinder end effect, wall effect, the effect of air currents and the reflection due to the thickness of the aquarium wall. Our technical breakthrough involves using the underwater lens to minimize the wall effect and avoid the wall reflection.

For high SG values approaching the theoretical maximum, as shown in figure 5, it was challenging to make the cylinder float, as even small perturbations would cause sinking. The difficulty in maintaining flotation for heavy cylinders is consistent with our observations that hyponeuston have safety factors between 2 and 8.

The instability of high SG experiments may be due to the nature of the net vertical force. For example, the saddle-node bifurcation observed in figure 6b,d points towards the relative change in the regime of stability for the stable branch (blue). As SG increases, the stable and unstable branches come closer together, which results in reduced stability of the equilibrium condition. The reduction in stability stems from the fact that a smaller perturbation of the floating object can transiently change the meniscus angle beyond the unstable branch (red), leading to loss of equilibrium and the object sinking underwater. This reduction in stability can explain the precarious nature of the floating equilibrium as the density of the object increases.

Other sources of experimental error include the angle measurements, which showed variability, even for identical samples, due to asymmetry between left and right sides of the cylinder. The samples were not perfectly axisymmetric, with a lower centre of mass and the presence of small air bubbles inside. These non-uniformities, combined with artefacts in filming and image analysis, likely contributed to errors in the angle measurements.

Our simple two-dimensional cylinder model is effective for understanding basic flotation mechanics but does not fully capture the complexities of live animal flotation. The regime diagram in figure 3g was constructed under the assumption of a cylindrical shape. However, many aquatic animals deviate from this geometry. For example, leeches utilize suction pads that can be better approximated as discs, while snails and planarians have irregular body shapes. Moreover, some animals employ additional mechanisms, such as mucus and air bubbles, to aid flotation. This likely explains why the SG of snails was measured to be less than 1 in our regime diagram. Previous studies have shown that purple snails (Janthina) use mucus-stabilized air bubbles for flotation and can even carry air bubbles within their shells to stay buoyant [31]. Future work incorporating these complexities could enhance the predictive power of flotation models for a wider range of organisms.

6. Conclusion

In this study, we investigated the flotation of hyponeuston with special emphasis on blackworms. We visualized meniscus profiles and explored the effects of corrugation on flotation. Our findings demonstrated that the corrugations did not increase vertical weight support. Using scaling arguments, we determined the safety factors of flotation for various hyponeuston. This study highlights the subtle interplay between body geometry, surface tension and buoyancy, offering insights into the adaptations of organisms inhabiting the air–water interface.

Ethics. This work did not require ethical approval from a human subject or animal welfare committee.

Data accessibility. Data are available from Zenodo: [32].

Declaration of AI use. We have not used AI-assisted technologies in creating this article.

Authors' contributions. S.K.: data curation, formal analysis, investigation, methodology, validation, visualization, writing—original draft; H.T.: data curation, formal analysis, investigation, methodology, validation, visualization, writing—original draft; N.H.: investigation, methodology, writing—original draft; I.T.: conceptualization, investigation, methodology, writing—original draft; S.B.: conceptualization, funding acquisition, project administration, supervision; D.H.: conceptualization, funding acquisition, project administration, supervision, writing—review and editing.

All authors gave final approval for publication and agreed to be held accountable for the work performed therein.

Conflict of interest declaration. We declare we have no competing interests.

Funding. This material was supported by the NSF Physics of Living Systems student network. S.B. acknowledges funding support from the NSF Grants CAREER 1941933 and PHY-2310691.

References

1. Banse K. 1975 Pleuston and neuston: On the categories of organisms in the uppermost pelagial. *Int. Rev. ges. Hydrobiol. Hydrogr.* **60**, 439–447. (doi:10.1002/iroh.19750600401)
2. Marshall HG, Burchardt L. 2005 Neuston: its definition with a historical review regarding its concept and community structure. *Arch. Für Hydrobiol.* **164**, 429–448. (doi:10.1127/0003-9136/2005/0164-0429)
3. Rohilla P, O'Neil JN, Singh P, Ortega-Jimenez VM, Choi D, Bose C, Bhamla S. 2025 Interfacial vortex recapture enhances thrust in tiny water skaters. *bioRxiv* 2024–06. (doi:10.1101/2024.06.17.599397)
4. Jami L, Gustafson GT, Steinmann T, Piñeirua M, Casas J. 2021 Overcoming drag at the water-air interface constrains body size in whirligig beetles. *Fluids* **6**, 249. (doi:10.3390/fluids6070249)
5. Hu DL, Bush JWM. 2010 The hydrodynamics of water-walking arthropods. *J. Fluid Mech.* **644**, 5–33. (doi:10.1017/s0022112009992205)
6. Guthrie M. 2024 *Animals of the surface film*. vol. 12. London, UK: Pelagic Publishing Ltd.
7. Philamore H, Rossiter J, Stinchcombe A, Ieropoulos I. 2015 Row-bot: An energetically autonomous artificial water boatman. In *2015 IEEE/RSJ Int. Conf. on Intelligent Robots and Systems (IROS)*, Hamburg, Germany. New York, NY: IEEE. (doi:10.1109/IROS.2015.7353924)
8. Rafeeq M, Toha SF, Ahmad S, Razib MA. 2021 Locomotion strategies for amphibious robots-a review. *IEEE Access* **9**, 26323–26342. (doi:10.1109/access.2021.3057406)
9. Gould J, Valdez JoseW. 2021 Locomotion with a twist: aquatic beetle walks upside down on the underside of the water's surface. *Ethology* **127**, 669–673. (doi:10.1111/eth.13203)
10. Grant IF. 2002 Aquatic invertebrates. In *Ecological monitoring methods for the assessments of pesticide impact in the tropics* (ed. Grant IF), pp. 183–193. London, UK: The University of Greenwich.
11. Lee S, Bush JWM, Hosoi AE, Lauga E. 2008 Crawling beneath the free surface: water snail locomotion. *Phys. Fluids* **20**, 82106. (doi:10.1063/1.2960720)
12. Lee SC, Kim JH, Lee SJ. 2017 Floating of the lobes of mosquito (*Aedes togoi*) larva for respiration. *Sci. Rep.* **7**, 43050. (doi:10.1038/srep43050)
13. Loudet JC, Pouligny B. 2011 How do mosquito eggs self-assemble on the water surface? *Eur. Phys. J.* **34**, 1–17. (doi:10.1140/epje/i2011-11076-9)
14. Suzuki C, Takaku Y, Suzuki H, Ishii D, Shimozawa T, Nomura S, Shimomura M, Hariyama T. 2021 Hydrophobic-hydrophilic crown-like structure enables aquatic insects to reside effectively beneath the water surface. *Commun. Biol.* **4**, 708. (doi:10.1038/s42003-021-02228-5)
15. Drewes CD. 1990 Tell-tail adaptations for respiration and rapid escape in a freshwater oligochaete (*Lumbriculus variegatus* Mull.). *J. Iowa Acad. Sci.* **97**, 112–114.
16. Pfiester M, Kaufman PE. 2009 Drone fly, rat-tailed maggot Eristalis tenax (Linnaeus) (Insecta: Diptera: Syrphidae). *EDIS* **445**. (doi:10.32473/edis-in809-2009)
17. Tuazon H nd. 2024 Physically entangled collective behavior of aquatic worm blobs. Ph.D. dissertation, [Atlanta, GA]: Georgia Institute of Technology.
18. Tuazon H, Nguyen C, Kaufman E, Tiwari I, Bermudez J, Chudasama D, Peleg O, Bhamla MS. 2023 Collecting–gathering biophysics of the blackworm *Lumbriculus variegatus*. *Integr. Comp. Biol.* **63**, 1474–1484. (doi:10.1093/icb/icad080)
19. Tuazon H, Kaufman E, Goldman DI, Bhamla MS. 2022 Oxygenation-controlled collective dynamics in aquatic worm blobs. *Integr. Comp. Biol.* **62**, 890–896. (doi:10.1093/icb/icac089)
20. Drewes CD, Fourtner CR. 1989 Hindsight and rapid escape in a freshwater oligochaete. *Biol. Bull.* **177**, 363–371. (doi:10.2307/1541596)
21. Rota E. 2022 How the discovery of oligochaete regeneration during the enlightenment was pivotal to the advancement of annelid research. *Zool. J. Linn. Soc.* **196**, 1–24. (doi:10.1093/zoolinnean/zlab111)
22. Patil VP, Tuazon H, Kaufman E, Chakrabortty T, Qin D, Dunkel J, Bhamla MS. 2023 Ultrafast reversible self-assembly of living tangled matter. *Science* **380**, 392–398. (doi:10.1126/science.ade7759)
23. Vella D, Lee DG, Kim HY. 2006 Sinking of a horizontal cylinder. *Langmuir* **22**, 2972–2974. (doi:10.1021/la0533260)
24. Greenhow M, Moyo S. 1997 Water entry and exit of horizontal circular cylinders. *Phil. Trans. R. Soc. Lond. A* **355**, 551–563. (doi:10.1098/rsta.1997.0024)
25. Vella D, Lee DG, Kim HY. 2006 The load supported by small floating objects. *Langmuir* **22**, 5979–5981. (doi:10.1021/la060606m)
26. Vella D. 2015 Floating versus sinking. *Annu. Rev. Fluid Mech.* **47**, 115–135. (doi:10.1146/annurev-fluid-010814-014627)
27. Rapacchietta AV, Neumann AW, Omenyi SN. 1977 Force and free-energy analyses of small particles at fluid interfaces. *J. Colloid Interface Sci.* **59**, 541–554. (doi:10.1016/0021-9797(77)90050-9)
28. Keller JB. 1998 Surface tension force on a partly submerged body. *Phys. Fluids* **10**, 3009–3010. (doi:10.1063/1.869820)
29. Mansfield EH, Sepangi HR, Eastwood EA. 1997 Equilibrium and mutual attraction or repulsion of objects supported by surface tension. *Phil. Trans. R. Soc. Lond. A* **355**, 869–919. (doi:10.1098/rsta.1997.0049)
30. Hu DL, Chan B, Bush JWM. 2003 The hydrodynamics of water strider locomotion. *Nature* **424**, 663–666. (doi:10.1038/nature01793)
31. Feldmann D, Das R, Pinchasik B. 2021 How can interfacial phenomena in nature inspire smaller robots. *Adv. Mater. Interfaces* **8**, 2001300. (doi:10.1002/admi.202001300)
32. Kim S, Tuazon H, Ha N, Tiwari I, Bhamla S, Hu D. 2025 Original Image and Codes for Floating Cylinders, Mimics of Aquatic Worms. In Flotation of Aquatic Worms and Other Hyponeuston. Zenodo. (doi:10.5281/zenodo.14773065)